N. Kamariah, D. Kalebic, P. Xanthopoulos, R. Blannin, F. P. Araujo, S.-F. Koelewijn, W. Dehaen, K. Binnemans, J. Spooren, *Minerals Engineering*, 183, **2022**, 107587.
https://doi.org/10.1016/j.mineng.2022.107587

# Conventional versus Microwave-Assisted Roasting of Sulfidic Tailings: Mineralogical Transformation and Metal Leaching Behavior

Nor Kamariah[1,2], Demian Kalebic[2], Panagiotis Xanthopoulos[2], Rosie Blannin[3], Fernando P. Araujo[4], Steven-Friso Koelewijn[1], Wim Dehaen[2], Koen Binnemans[2], Jeroen Spooren[1,*]

[1] Sustainable Materials Management, Flemish Institute for Technological Research (VITO n.v.), Boeretang 200, 2400 Mol, Belgium

[2] KU Leuven, Department of Chemistry, Celestijnenlaan 200F, Box 2404, 3001 Leuven, Belgium

[3] Helmholtz Institute Freiberg for Resource Technology, Helmholtz-Zentrum Dresden-Rossendorf, Chemnitzer Str. 40, 09599 Freiberg, Germany

[4] KU Leuven, Department of Earth and Environmental Sciences, Celestijnenlaan 200E, Box 2410, 3001 Leuven, Belgium

[*] Corresponding author: jeroen.spooren@vito.be; tel +32 14 335633

Keywords: Conventional roasting, microwave roasting, sulfidic tailings, mineralogical transformation, water leaching

## Abstract

Roasting is often required to convert sulfidic minerals into their sulfate and/or oxide forms with the aim to increase the extractability of targeted metals. In this study, sulfidic tailings of Neves Corvo Cu-Zn-Pb-mine (Portugal) underwent conventional roasting (CR) and microwave-assisted roasting (MR) to compare the effect of both heating technologies on the roasting behavior. Upon roasting in air, transformations of mineral phases in the tailings were studied by different techniques using quantitative X-ray diffraction, mineral liberation analysis, Raman spectroscopy and thermogravimetry–differential scanning calorimetry coupled to mass spectrometry. Also, the leaching behavior of elements from the roasted tailings was assessed in water. It was shown that CR and MR induce different reaction pathways for mineral transformations during roasting. While CR led to indirect pyrite oxidation through intermediate sulfate formation, direct pyrite oxidation was the main transformation pathway during MR. This change in reaction pathway can be attributed to the mineral-selective heating induced by microwaves, which in particular accelerates the oxidation rate of pyrite. In agreement with the proposed roasting mechanism, the leaching behavior in water showed that CR resulted in a higher extraction of Cu, Zn, Pb, As and Fe from the tailings – since their sulfate phases are more abundant – compared to MR at the same roasting temperature. Overall, tailings treated by CR and MR within the temperature ranges of 500 °C to 550 °C for 1 hour gave optimal leaching efficiencies of the studied metals (water leaching at room temperature for 30 min; stirring speed of 600 rpm; solid-to-liquid ratio of 10 $\mathrm{mL} \cdot \mathrm{g}^{-1}$). Furthermore, thermodynamic equilibrium calculations showed that hydrolysis of soluble Fe(III) species strongly controls the pH of the leachates. In comparison to MR tailings, more acidic leachates were generated for CR tailings because of a more pronounced formation of ferric sulfate.

## Introduction

Roasting plays an important role in pyrometallurgical and hydrometallurgical routes to enable the extraction of metals from sulfidic minerals through oxidation into their respective sulfate and/or oxide minerals [1][2]. In pyrometallurgy, roasting is widely applied as a pretreatment, for instance, to recover gold from refractory gold ores and concentrates [3], to oxidize pentlandite for nickel extraction [4] and to eliminate the sulfur content of sphalerite concentrate prior to zinc extraction [5]. In many hydrometallurgical processes, particularly in which bioleaching of chalcopyrite or oxidative leaching of bornite and covellite are not capable of leaching metals efficiently, roasting is a key pretreatment step for conversion of sulfides into oxides before acid or ammoniacal leaching can be carried out efficiently [6].

For conventional roasting (CR) in the industry, a rotary kiln, fluidized bed reactor or shaft furnace is being used [3][5]. Although not applied on industrial scale yet, microwave-assisted roasting (MR) has gained much research interest in recent years [7][8]. In contrast to conventional heating, microwave-assisted heating is fast, non-contact, volumetric and selective [9][10], and consumes less energy [11][12]. These advantages can be exploited to improve the roasting performance [13]. Previous studies reported prospective applications of MR to treat sulfide materials, such as gold concentrate and mixed oxide-sulfide zinc ores, in which microwaves were capable of increasing the reaction rate of gold desulfurization and zinc leaching, respectively [8][12].

The increasing demand for sulfidic metal ores, together with the depletion of the high-grade ores [14][15], makes the recovery of valuable metals from low-grade and more complex sulfidic ores of increasing importance. Sulfidic tailings, being a major extractive waste generated during the production of Cu, Zn and Pb, amongst others, can serve as an additional resource to help fulfil the global metal demand. Sulfidic tailings may contain significant amounts of base and precious metals, such as Ni, Cu, Zn, Au and Ag, that were not recovered by froth flotation during beneficiation [16]. One study reported that beneficiation plants which process ore concentrates containing (0.5 to 2) wt % of Cu lose up (25 to 35) wt % of the Cu content to the tailings [17]. Similar to sulfide primary ores and concentrates, metal extraction from sulfidic tailings also requires roasting to convert stable sulfide minerals to their oxides prior to leaching [18][19].

To selectively extract targeted metals from materials with heterogenous chemical compositions, *e.g.* sulfidic tailings, it is important to understand the mineralogical transformation that occurs during roasting. Controlled roasting may enhance extraction of desirable metals while minimizing dissolution of unwanted metals. Although several studies have investigated the roasting of certain sulfide minerals, to the best of our knowledge, no specific study has been conducted on mineralogical transformations within sulfidic tailings during CR *versus* MR. To make recovery of metals from waste tailings economically viable, there is a need to improve the process economics and to increase metal extraction efficiencies, thereby achieving near-zero waste processing of such low-grade raw materials [15]. The results of this study are valuable to find optimal roasting conditions, during both the conventional and microwave-assisted heating, to achieve efficient metal extraction from sulfidic tailings. In particular, we investigated and compared the roasting behavior of sulfidic tailings as a function of roasting temperatures in CR and MR. Multiple characterization techniques were applied to gain insight into the occurring roasting mechanisms. Finally, mobilization of the studied metals (Cu, Zn, Pb as valuable metals; As as toxic metalloid; Fe as metal impurity) in the roasted tailings were evaluated by water leaching.

## Experimental

### Materials

The sulfidic tailings samples were kindly provided by SOMNICOR Lunding Mining S.A. from the tailings storage facilities of the company located in Neves Corvo mine area of the Iberian Pyrite Belt (Portugal). Milli-Q® water (18.2 MΩ.cm at 25 $^{o}$C, TOC < 5 ppb) was used as a solvent during water leaching. Analytical grade 37 % HCl, 38 % $HBF_4$, 65 % $HNO_3$ (*Fisher Scientific*) and multi-element standards (*LabKingS*) were used to digest solid samples and prepare standard solutions for ICP-OES analyses.

**Analyses**

X-Ray Diffraction (XRD) using a *PANalytical Empyrean Diffractometer* was performed to determine crystallographic phase composition of the materials before and after roasting. The diffractometer was operated at 40 kV and 40 mA with a cobalt anode and was equipped with a graphite monochromator and a proportional detector. Continuous mode scans with a scanning speed of 0.010° · $s^{-1}$ and a step size of 0.04° were performed in the 2θ range between 5° and 120°. *HighScore Plus* software was used for qualitative and quantitative analyses of the diffractograms. The mineralogical composition was quantified by Rietveld refinement to yield an RWP (weighted profile R-factor) value of <10 % with the GOF (goodness of fit) values within the range of 4.91–6.00.

The original tailings sample (0.25 g) was digested using 3 mL of HCl, 1 ml of $HBF_4$ and 1 mL of $HNO_3$ at 105 °C for 2 hours in *Digiprep Block Digestion System* (SCP Science). The elemental composition of the tailings and metal concentrations in pregnant leach solutions (PLS) were analysed by Inductively Coupled Plasma Optical Emission Spectroscopy (ICP-OES) on a *Perkin Elmer® Avio 500* instrument.. Liquid samples were diluted with 5 % of $HNO_3$ and then measured in triplicate.

Thermogravimetry-Differential Scanning Calorimetry (TG-DSC) using a *Netzsch STA 449 C Jupiter®* and coupled to a quadrupole *Hiden ExQ* mass spectrometer for gas analysis were applied to understand thermal characteristics and decomposition products of the tailings. Approximately 50 mg of powdered sample was placed in an alumina crucible and heated from 25 °C to 1200 °C in air with flow rate of 50 mL · $min^{-1}$ and at a heating rate of 10 °C · $min^{-1}$.

Raman analyses were conducted using a *Horiba Jobin-Yvon LabRAM HR Evolution* spectrometer. Spectra were measured using a 100× long working distance objective (*Olympus LMPLFLN, NA 0.8*) coupled to an *Olympus BX41* confocal microscope. Raman spectra were acquired and treated with the *LabSpec 6.5.2* software. Spectrometer X-axis calibration (Raman shift) was performed using the NIST certified *Horiba SP-RCO* objective (polystyrene Raman peak at 1001 $cm^{-1}$). Visible and hidden peaks were fitted with Voigt functions (convolution of Gaussian and Lorentzian curves) using the *Fityk* software [20][21], v.1.3.1. Further details on the Raman instrumentation, methodology, and calibration procedures used in this study are provided by Araujo et al. [21].

Mineral Liberation Analysis (MLA), a scanning electron microscopy (SEM)-based automated image analysis program, was performed to investigate the mineral phases present in the original tailing samples as well as those produced during MR. The MLA analyses were performed on an *FEI Quanta 650 F* field emission SEM (FE-SEM) equipped with two *Bruker*

*Quantax X-Flash 5030* energy-dispersive X-ray (EDX) detectors and the MLA software suite version 3.0. The grain-based X-ray mapping (GXMAP) measurement mode was used [22][23].

For MLA, polished grain mounts, with a diameter of 30 mm, were prepared by mixing 1 g of sample with pure graphite powder and embedding the mixture in epoxy resin. To prevent issues associated with segregation of particles in the resin, due to differential settling based on density and particle size, the sample block was sliced, vertically rotated by 90° and remounted in epoxy resin before polishing [24]. Two grain mounts were made for the original tailing sample, as well as for the MR samples of 400 °C, 500 °C and 600 °C, to improve the measurement statistics and identify a sufficient number of the minerals of interest which are typically present in minor abundances in the tailing materials. The operating conditions used for SEM and MLA are listed in the supplementary material Table S1.

The compilation of the mineral list for classification of the MLA results was straightforward for the original tailings material. However, due to the fine-grained nature of the materials, mixed spectra were abundant. As is standard procedure in automated mineralogy, manually created mixed spectra between common minerals were added to the mineral reference list in ratios of 1:2 and 2:1 (cf. Bachmann et al. [25] and Kern et al. [26] for this approach). The classified data were processed with several software scripts to remove the mixed spectra and de-agglomerate the particles. For the MR samples, compilation of the mineral list was more challenging. The roasted phases are not typical mineral phases and are therefore not available in any standard reference list. Therefore, the roasted phases had to be identified in the samples, X-ray spectra collected and the composition quantified. However, the irregular surfaces of the phases that formed during roasting made it difficult to obtain representative X-ray spectra and accurately quantify the composition. Due to these difficulties, standard densities and compositions of the identified roasted phases, i.e. sulfates and oxides, were used instead. Therefore, the results should be viewed as semi-quantitative in nature. In order to estimate the uncertainties on the MLA-derived data, bootstrap resampling was performed. This involved randomly resampling the original dataset 1000 times to produce 1000 possible datasets, followed by the calculation of the median values and standard deviation of the relevant results. See Blannin et al. [27] for a detailed description of the method followed.

Thermodynamic equilibrium calculations by the GEM module of the *HSC Chemistry* software (version 8.2.0) were performed to determine the equilibrium pH at 25 °C of a solution with an initial input of $Fe_2(SO_4)_3$. Detailed information on this modelling is given in the supplementary material Table S2.

## Experimental Methods

Before roasting, the original tailings were dried at 40 °C to constant mass under flowing nitrogen to avoid oxidation. The dried tailings samples were crushed into fine powders (with a mean particle size of 19 µm ± 1 µm, a $d_{50}$ = 7.7 µm ± 0.3 µm and $d_{90}$ = 57 µm ± 6 µm (*Microtrac S3500*)) with a mortar and a pestle and then roasted in duplicate at selected temperatures in air. For CR the samples were placed in porcelain crucibles that were heated in a conventional muffle induction furnace (*Nabertherm*) from room temperature to the set temperatures (450 °C, 500 °C, 550 °C or 600 °C), at a heating rate of 2 $°C \cdot min^{-1}$ and a dwell time of 60 min [18]. Concurrently, for MR the samples were placed in alumina crucibles, which were heated in a microwave furnace (*Milestone PYRO advance*) from room temperature to the set temperatures (400 °C, 500 °C, 550 °C or 600 °C) at a ramp time of 30 min and a dwell time of 60 min. The samples were weighed before and after roasting to determine the mass loss (*ML*):

$$ML(\%) = \frac{m_i - m_f}{m_i} \times 100 \qquad \text{(Eq. 1)}$$

where $m_i$ is the initial mass of the sample before roasting (in g) and $m_f$ the final mass of the sample after roasting (in g).

Water leaching experiments of the CR and MR samples were performed at room temperature (± 25 °C) for 30 min on a magnetic stirring plate (at 600 rpm) at a liquid-to-solid ratio (L/S) of 10 $mL \cdot g^{-1}$ (5 mL of water; 0.5 g of sample). After leaching, the solid residues were separated from the PLS by vacuum filtration. The PLS and dried solid residues were prepared for ICP-OES analysis. The leaching efficiency ($E_L$) was calculated following Eq. 2.

$$E_L(\%) = \frac{C_M \times V_S}{m_r \times C_r} \times 100 \qquad \text{(Eq. 2)}$$

where $C_M$ is the metal concentration in the PLS after leaching (in $mg \cdot L^{-1}$ ), $V_S$ is the volume of solvent (i.e. Milli-Q® water) used for leaching (in L), $m_r$ is the mass of the roasted sample used for leaching (in kg), and $C_r$ is the metal concentration in the roasted sample before leaching (in $mg \cdot kg^{-1}$).

# Results and Discussion

## Chemical and Mineralogical Characteristics of Sulfidic Tailings

Chemical analysis identified Fe and S as the main elements in the sulfidic tailings, as shown in Table 1. Valuable metals (Zn, Cu, Pb) and toxic metalloid (As) were present at low concentrations.

**Table 1** Elemental composition of the Neves Corvo sulfidic tailings as measured by ICP-OES.[a]

| Element | Concentration (ppm) |
|---|---|
| Fe | 264000 |
| S | 244500 |
| Zn | 10360 |
| Cu | 3515 |
| Pb | 3970 |
| As | 4810 |

[a] tested in duplicate and reported data are mean values

In agreement with the chemical analysis, mineralogical composition revealed pyrite being the dominant mineral phase (43.7 wt %) of the sulfidic tailings, followed by quartz (28.9 wt %) and chamosite (21.3 wt %) (Fig. 1). Small quantities of siderite (2.7 wt %), muscovite (2.6 wt %) and tetrahedrite (0.8 wt %) were identified as well (supplementary material Table S3). While some Zn-bearing mineral was detectable, it could not be accurately quantified by Rietveld refinement. Additionally, due to their low concentrations (see Table 1), neither Cu- nor Pb-bearing minerals could be identified by XRD.

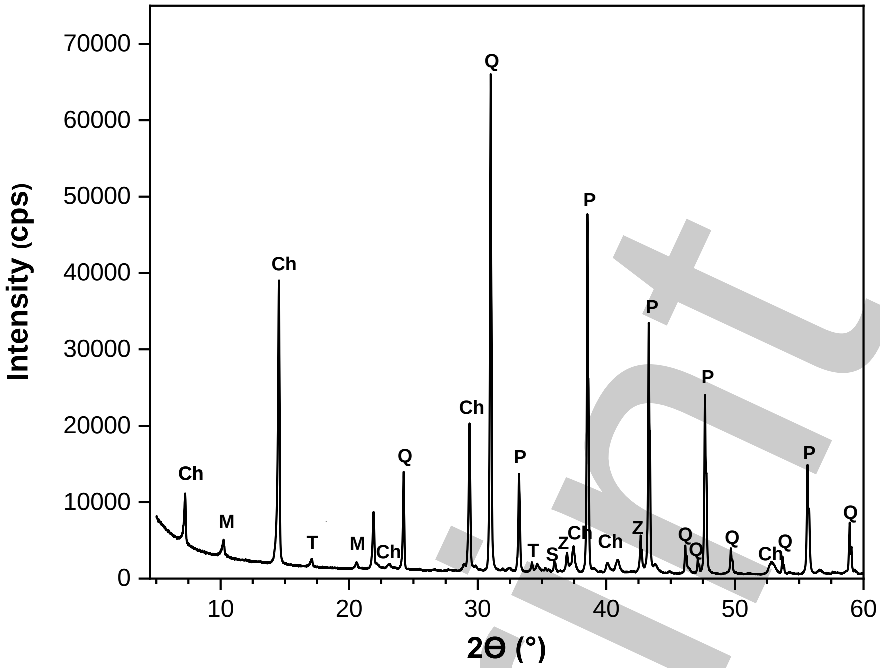

**Fig. 1** XRD diffractogram of the Neves Corvo sulfidic tailings (Ch-Chamosite; M-Muscovite; P-Pyrite; Q-Quartz; S-Siderite; T-Tetrahedrite; Z-Zinc bearing mineral (sphalerite))

To complement the mineral phase identification obtained by the XRD analysis, Raman micro-analysis was applied using Raman spectrometry coupled with a confocal optical microscope. The collected Raman spectra confirmed the presence of pyrite, characterized by two dominant pyrite bands at 342 $cm^{-1}$ and 377 $cm^{-1}$, as well as a minor band at 429 $cm^{-1}$ (Fig. 2A), with full width at half maximum (FWHM) of 1.6 $cm^{-1}$, 2.2 $cm^{-1}$, and 4.9 $cm^{-1}$, respectively. Those bands respectively correspond to the $A_g$, $E_g$ and $F_g$ Raman modes and agree with similar results reported by earlier studies [28][29][30]. Some analyses showed broader peaks that are slightly shifted to lower wavenumbers (Fig. 2B). The $A_g$, $E_g$, and $F_g$ bands are observed at 340 $cm^{-1}$, 375 $cm^{-1}$, and 426 $cm^{-1}$, with FWHM of 3.6, 4.6, and 5.7 respectively. Additionally, a very broad band is observed at 287 $cm^{-1}$ with FWHM of 10.5. Rarely, different spectral shapes were observed showing only two of the characteristics pyrite bands ($A_g$ and $E_g$) shifted to 371 and 342 $cm^{-1}$ (Fig. 2C).

Additionally, other peaks appear at 257 $cm^{-1}$, 269 $cm^{-1}$ and 280 $cm^{-1}$, and a very broad band at 457 $cm^{-1}$. The shift of main pyrite bands to different positions can be attributed to the incorporation of minor or trace elements to the pyrite structure [31][32]. The incorporated elements will slightly distort the crystal lattice of pyrite, due to their different ionic radii in relation to Fe, leading to different bond lengths and vibration energies, which causes the downshift and increase in the FWHM of the Raman bands.

The shifted bands to lowered wavenumbers, accompanied by the appearance of a broad band at 287 $cm^{-1}$ in Fig. 2B, indicate some assimilation of Cu into pyrite. Although the broad band at 287 $cm^{-1}$ resembles the main band of chalcopyrite [[30] the large FWHM indicates some level of disorder in the Cu-Fe substitution. Broad low-intensity bands appearing from 257 $cm^{-1}$ to 280 $cm^{-1}$ have also been observed in Fig. 2C. These resemble arsenopyrite bands [31], which could also indicate some incorporation of As in pyrite.

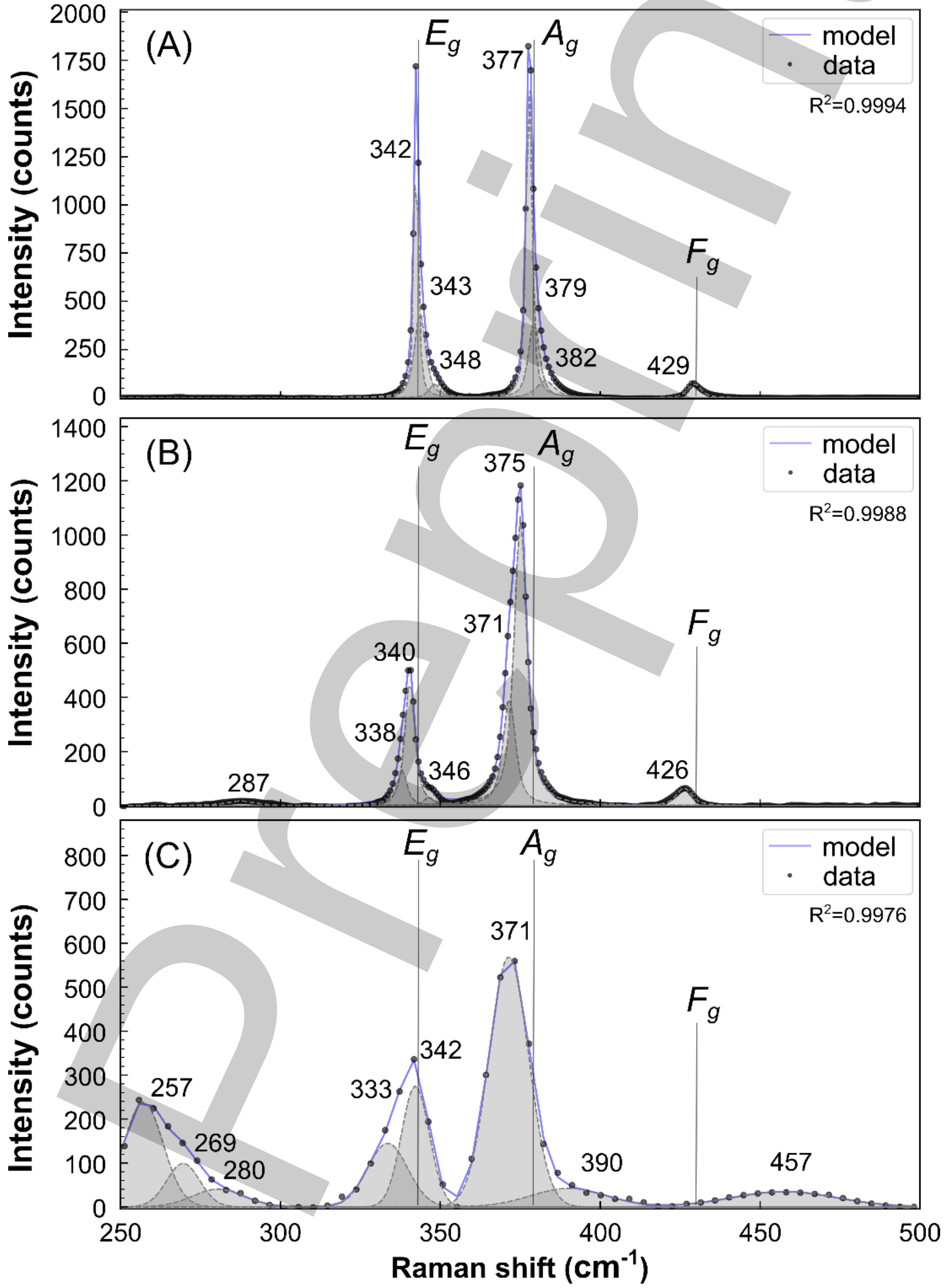

**Fig. 2** Raman spectra of original sulfidic tailings for selected regions showing (A) the typical pyrite spectrum, (B) downshifted bands with new bands resembling chalcopyrite Raman peaks,

and (C) multiple low wavenumber bands that resemble Raman peaks from arsenopyrite. Fitting validation between data (dotted lines) and model (full line) after fitting peaks (shaded) are represented by $R^2$ (coefficient of determination). The vertical lines ($E_g$, $A_g$, and $F_g$) represent the ideal position for the respective Raman bands in pyrite [28].

In addition to Raman micro-analysis, MLA was employed to identify mineral phases, in particular those present in low abundance, and to provide information on the deportment of the metals of interest. A total of 43 mineral phases were identified in the tailings, which were subsequently grouped into 13 mineral groupings (supplementary material Table S4). The modal mineralogy of the original tailings is given in Table 4 for the 13 mineral groupings. As could be expected from the geology and mineralogy of the Neves Corvo ore [33], the mineralogy of the tailings is dominated by silicates and oxides (~50 wt %), comprised mainly of quartz, feldspars and chlorites, as well as pyrite (~46 wt %) and other sulfide minerals which host the metals of interest. These results corroborate the findings of XRD and Raman micro-analysis.

Sulfide minerals are the dominant hosts of Cu, Zn, Pb, As and Fe in the tailings. The deportments of these metals are given in Table 2, as calculated from the modal mineralogy. Cu is present primarily in chalcopyrite and sulfosalts (tennantite and tetrahedrite) and minor amounts in other Cu sulfides (bornite, covellite and bournonite). Sphalerite and galena are the hosts of Zn and Pb, respectively, while As mainly occurs in arsenopyrite, with minor amounts contributed by sulfosalts. Pyrite is the dominant sulfide mineral and hosts the majority of the Fe (82.7 wt %) and S (96.9 wt %). Considering the dominance of these sulfide minerals, roasting is foreseen to be essential to extract more easily the metals from the tailings.

**Table 2** Deportment of Fe, S, Cu, Zn, Pb and As (in wt %) in the Neves Corvo sulfidic tailings[b]

| Mineral Grouping | Fe | S | Zn | As | Cu | Pb |
|---|---|---|---|---|---|---|
| Arsenopyrite | 0.7 ± 0.1 | 0.4 ± 0.0 | | 95.4 ± 1.4 | | |
| Pyrite | 82.7 ± 0.5 | 96.9 ± 0.3 | | | | |
| Chalcopyrite | 0.7 ± 0.1 | 0.8 ± 0.1 | | | 84.0 ± 3.4 | |
| Other Cu sulfides | | | | | 1.7 ± 0.9 | |
| Galena | | 0.1 ± 0.0 | | | | 100 ± 0.0 |
| Sphalerite | 0.1 ± 0.0 | 1.8± 0.3 | 100 ± 0.0 | | | |
| Sulfosalts | | 0.1± 0.0 | | 4.6 ± 1.4 | 14.3 ± 3.8 | |
| Fe oxides | 0.3 ± 0.1 | | | | | |
| Fe carbonate | 4.4 ± 0.3 | | | | | |

[b] mean content from 1000 bootstrap resampling simulations ± two standard deviations (σ) to show the 95 % confidence level

## Thermal Decomposition of Sulfidic Tailings

TG-DSC in air was conducted to examine the thermal behavior and stability of minerals present in the sulfidic tailings. Moreover, the effluent gas released during TG-DSC was monitored by MS. Of particular interest were gaseous decomposition products characterized by mass-to-charge (m/z) ratios of 18 ($H_2O$), 44 ($CO_2$), 48 (SO), 64 ($SO_2$) and 80 ($SO_3$).

The measured TG and DSC curves (Fig. 3A) generally coincided with those reported in earlier detailed thermogravimetric and calorimetric studies on the roasting of pyrite tailings and/or chalcopyrite rich ores [34-35]. Two main decomposition regions were observed. The first region (between 382 °C to 450 °C) was marked by a mass loss of approximately 10 %. Based on the DSC, this mass loss coincides with a significant exothermic heat flow that reaches a maximum of -130 kW · $g^{-1}$. MS data (Fig. 3B) confirmed that this first region is the off-gassing of $SO_x$. The release of $H_2O$ and $CO_2$ in this temperature range can be assigned to the transformation of carbonate and hydroxide phases into sulfate phases, as we have shown in the previous work [18]. On closer inspection, two distinct peaks/signals are discernable in both the exothermic DSC peaks and $SO_x$ MS signals, wherein the first MS signal at 376 °C can be associated to the decomposition of pyrite ($FeS_2$) to troilite (FeS) (Eq. 3 [18]).

In the second region, comparably a small portion of gasses was also released at 535 °C, corresponded to the decomposition of troilite (Eq. 4-5) [18], which was accompanied by the second slope in TGA curve. Around this temperature (500 °C to 550 °C), sulfate formation may also take place following Eq. 4 and 6 [18] [35], although the gained mass could not be observed due to simultaneous release of $SO_2$. In fact, 535 °C signals the onset of the sulfate decomposition to allow the further oxidation of $Fe^{2+}$ to $Fe^{3+}$ in the form of hematite ($Fe_2O_3$) following Eq. 7 [34-35]. However, the expected release of $SO_3$ from this step could not be observed in the MS signal due to its rapid fragmentation into $SO_2^+$ and $SO^+$ when applying electron impact ionization during the measurement [36]. The presence of the less dominant SO peak in Fig. 3B (making the ratio close to 0.5 for SO:$SO_2$) is an indication for the decomposition of oxidative sulfur species [37]. Sulfur dioxide was further released from the residual structure, resulting in the mass loss up to 3.5 % at 1200 °C. Finally, in the temperature range 725 °C to 825 °C remaining carbonate phases decomposed.

$FeS_2\,(s) + O_2\,(g) \rightarrow FeS\,(s) + SO_2\,(g)$ (Eq. 3)

$FeS\,(s) + 2\,O_2\,(g) \rightarrow FeSO_4\,(s)$ (Eq. 4)

$3\,FeS\,(s) + 5\,O_2\,(g) \rightarrow Fe_3O_4\,(s) + 3\,SO_2\,(g)$ (Eq. 5)

$2\,FeS_2\,(s) + 7\,O_2\,(g) \rightarrow Fe_2(SO_4)_3\,(s) + SO_2\,(g)$ (Eq. 6)

$2\,FeSO_4\,(s) \rightarrow Fe_2O_3\,(s) + SO_2\,(g) + SO_3\,(g)$ (Eq. 7)

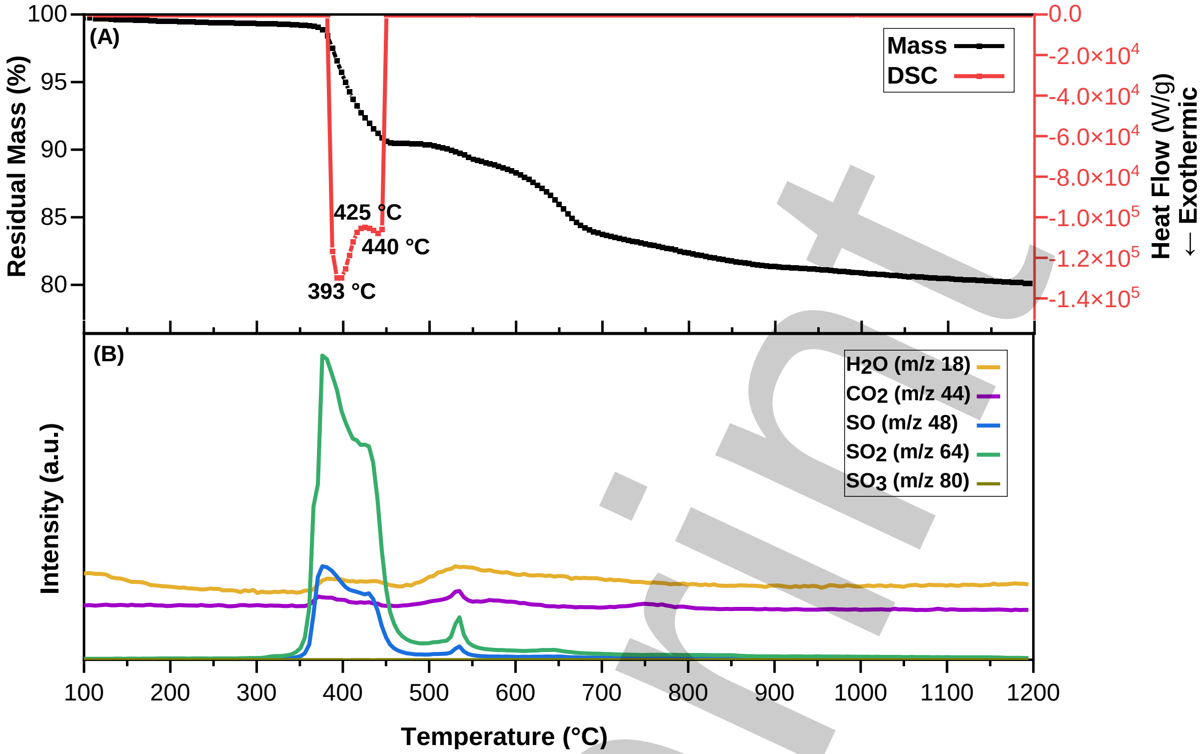

**Fig. 3** TG-DSC (A) and MS (B) analysis of the Neves Corvo sulfidic tailings

### Conventional Roasting (CR) vs Microwave-Assisted Roasting (MR)

To allow for the extraction of valuable metals such as Cu, Zn and Pb from the sulfidic tailings, roasting is used to transform the stable sulfide minerals into more water-soluble sulfates and/or oxide minerals. Yet, at the same time, the large quantity of pyrite will be inevitably roasted as well. To gain insight into the roasting mechanisms occurred during CR and MR, the mineralogical transformation as a function of roasting temperature was first studied via quantitative XRD. Different compositions of Fe-containing mineral phases were observed after either CR or MR. While Zn-bearing minerals were detected by XRD, unfortunately, due to their low concentration, Cu- and Pb-bearing mineral phases could not be identified. Therefore, as a representative alternative, the roasting of pyrite as the abundant sulfide mineral was monitored instead to indirectly predict the roasting mechanism of Cu, Zn, Pb and As-bearing sulfide minerals.

Mineral compositions after CR and MR are illustrated in Fig. 4. Compared to non-roasted tailings, the pyrite phase was greatly reduced in the roasted tailings at all selected temperatures, indicating that oxidation of sulfide minerals already occurred at 450 °C for CR and at 400 °C for MR. While pyrite content decreased, magnetite ($Fe_3O_4$) and hematite ($Fe_2O_3$) contents arose in the roasted tailings, corresponding to the oxidation products of $FeS_2$ and conforming the chemical reactions of Eq. 5 and 7, respectively.

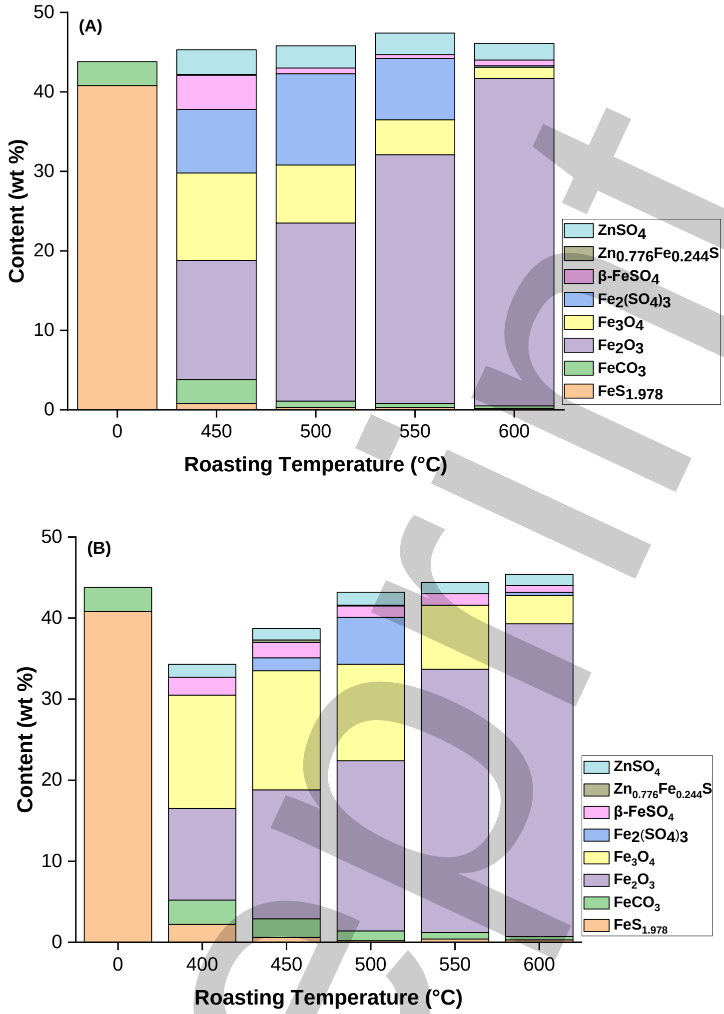

**Fig. 4** Quantification of Fe and Zn-containing mineral phases after (A) CR (fixed heating rate of 2 °C · $min^{-1}$) and (B) MR (fixed ramp time of 30 min) at selected temperatures for 1 h compared to the non-roasted Neves Corvo sulfidic tailings (0 °C referred to fresh tailings before roasting)

Compared to MR, a larger amount of iron sulfate phases and a lesser amount of magnetite ($Fe_3O_4$) were observed for CR. These differences in composition indicate that dissimilar reaction pathways are preferred during CR and MR. Beside direct oxidation to iron oxides, which was confirmed by the presence of magnetite and hematite during CR, pyrite has partially undergone oxidation to ferrous ($FeSO_4$) and ferric sulfate ($Fe_2(SO_4)_3$) to a larger extent than during MR, proposedly following Eq. 3-4 and 6-9 [18, 34-35, 38-39] . Sulfate species were more observable in CR at 400 °C to 550 °C, whereas oxides prevailed at 600 °C. This agrees with previous studies reporting $FeSO_4$ forms at relatively low temperatures and/or at slow heating rate, and decomposes to form more $Fe_2O_3$ at 550 °C and above [38][39]. On the other hand, $Fe_2(SO_4)_3$ could be formed from oxidation of $FeS_2$ or as a further oxidation product of troilite (FeS) and ferrous sulfate ($FeSO_4$).

*Proposed indirect pyrite oxidation through intermediate sulfates, prevalent during CR:*

$FeS_2 (s) + O_2 (g) \rightarrow FeS (s) + SO_2 (g)$ (Eq. 3)

$FeS (s) + 2 O_2 (g) \rightarrow FeSO_4 (s)$ (Eq. 4)

$2 FeS_2 (s) + 7 O_2 (g) \rightarrow Fe_2(SO_4)_3 (s) + SO_2 (g)$ (Eq. 6)

$2 FeSO_4 (s) \rightarrow Fe_2O_3 (s) + SO_2 (g) + SO_3 (g)$ (Eq. 7)

$2 FeSO_4 (s) + O_2 (g) + SO_2 (g) \rightarrow Fe_2(SO_4)_3 (s)$ (Eq. 8)

$Fe_2(SO_4)_3 (s) \rightarrow Fe_2O_3 (s) + 3 SO_3 (g)$ (Eq. 9)

On another note, a higher content of $Fe_3O_4$ after MR indicates that direct pyrite oxidation was the major reaction pathway followed. Contrary to CR (Fig. 4A), the content of ferric sulfate in MR became lower as the temperature increased, with the exception of roasting at 500 °C (Fig. 4B). This may suggest that direct oxidation route of ferrous sulfate-to-oxides is more preferred, rather than ferrous sulfate to ferric sulfate. As a result, $Fe_3O_4$ was quantified as the main intermediate product before it was fully oxidized to hematite ($Fe_2O_3$), following Eq. 3, 5, 10-11 [18, 35]. Other reactions could possibly occur but are not determined in this study.

*Proposed direct pyrite oxidation to oxides during MR:*

$FeS_2 (s) + O_2 (g) \rightarrow FeS (s) + SO_2 (g)$ (Eq. 3)

$3 FeS (s) + 5 O_2 (g) \rightarrow Fe_3O_4 (s) + 3 SO_2 (g)$ (Eq. 5)

$2 Fe_3O_4 (s) + 0.5 O_2 (g) \rightarrow 3 Fe_2O_3 (s)$ (Eq. 10)

$2 FeS_2 (s) + 5.5 O_2 (g) \rightarrow Fe_2O_3 (s) + 4 SO_2 (g)$ (Eq. 11)

The strong microwave absorption by pyrite induced selective fast heating of the pyrite phases to higher temperatures in the microwave furnace [40]. This consequently caused rapid thermal decomposition of the formed sulfates, thus promoting a fast sulfide-to-oxide mineral transition. In agreement with this hypothesis, Zhang et al. (2019) reported that temperature phase transition of high purity pyrite in the microwave heating was decreased by approximately 100 °C compared to the temperature in conventional heating, attributing it to short microwave heating time [41].

Moreover, QXRD showed the presence of a lower amount of zinc sulfate after MR compared to after CR (Fig. 4), indicating that the sulfate-to-oxide phase transition of sphalerite (ZnS) also occurred at a faster pace during MR. Given that most sulfide minerals are good microwave absorbers [42], such fast and selective heating during MR is expected to give a similar effect to chalcopyrite ($CuFeS_2$) and galena (PbS) as the respective main Cu and Pb-bearing minerals in the tailings.

The different roasting mechanisms can also be observed from the obtained mass loss and sulfur content. The formation and decomposition of sulfur during roasting resulted in mass losses (Fig. 5), which corresponded to the roasting temperatures set in the furnace. The calculated mass loss of the CR samples was comparable to the mass loss observed from the previously mentioned TGA measurement in the range of 450 °C to 600 °C. It should be noted that some deviations could be due to different temperature stability and air-flow between a conventional and a TGA furnace. At identical roasting temperatures, MR each time yielded a higher mass loss than CR, corresponding to the overall higher sulfur removal (in wt %) after MR (Table 3).

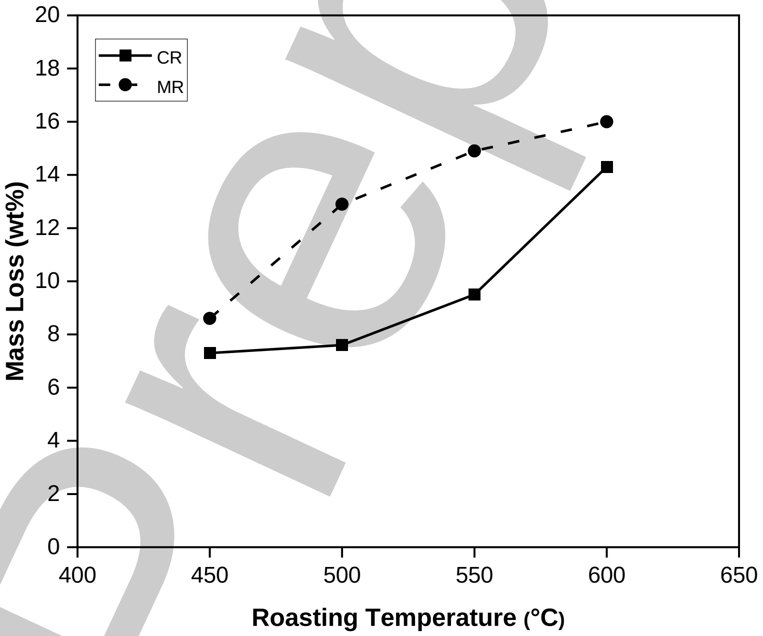

**Fig. 5** Mass loss of the CR and MR samples at each roasting temperature

**Table 3** Elemental analysis of the non-roasted and roasted tailings

| **Element** | **Non-Roasted Tailings (wt %)** | **Roasted Tailings (wt %)** | | | | | | | | |
|---|---|---|---|---|---|---|---|---|---|---|
| | | **CR (°C)** | | | | **MR (°C)** | | | | |
| | | 450 | 500 | 550 | 600 | 400 | 450 | 500 | 550 | 600 |
| Fe | 25.8 | 30.8 | 31.7 | 32.5 | 33.9 | 30.2 | 31.6 | 33.7 | 33.9 | 34.5 |
| S | 24.6 | 7.01 | 7.50 | 5.66 | 3.37 | 5.71 | 4.86 | 4.72 | 3.52 | 3.11 |
| Zn | 0.68 | 0.79 | 0.80 | 0.80 | 0.89 | 0.72 | 0.74 | 0.77 | 0.78 | 0.78 |
| As | 0.47 | 0.54 | 0.55 | 0.56 | 0.61 | 0.51 | 0.55 | 0.58 | 0.58 | 0.57 |
| Cu | 0.30 | 0.30 | 0.32 | 0.34 | 0.35 | 0.30 | 0.31 | 0.33 | 0.34 | 0.36 |
| Pb | 0.33 | 0.37 | 0.37 | 0.39 | 0.40 | 0.36 | 0.36 | 0.39 | 0.39 | 0.40 |

To obtain more detailed information on the mineral speciation for the minor Cu, Zn and Pb phases, MLA was performed on the MR samples. Due to the difficulties in collecting representative X-ray diffractograms of these roasted phases and quantifying their composition, the contents of these phases estimated by MLA should be viewed as semi-quantitative. The modal mineralogy of the MR samples is given in Table 4. Supplementary material Table S4 summarizes the mineral phases identified in the MR samples, and the mineral groupings applied. Phases identified by MLA include Fe, Cu and Zn sulfates, Cu and Zn oxides as well as some other alteration phases present in trace amounts. Supplementary material Table S5, S6 and S7 show the deportments of Fe, S, Cu, Zn and Pb in the MR samples.

**Table 4** Modal mineralogy of the Neves Corvo sulfidic tailings[b]

| **Mineral Grouping** | **Content (wt %)** | | | |
|---|---|---|---|---|
| | **Original Tailings** | **MR Tailings** | | |
| | | **400** °C | **500** °C | **600** °C |
| Silicates and oxides | 48.4 ± 0.8 | 53.1 ± 1.5 | 48.1 ± 1.5 | 46.0 ± 1.5 |
| Arsenopyrite | 0.5 ± 0.1 | 0.4 ± 0.0 | n.d.* | n.d.* |
| Pyrite | 45.5 ± 0.8 | 12.0 ± 1.0 | n.d.* | n.d.* |
| Chalcopyrite | 0.6 ± 0.1 | 0.3 ± 0.1 | n.d.* | n.d.* |
| Other Cu sulfides | n.d.* | 0.1 ± 0.0 | n.d.* | n.d.* |
| Galena | 0.1 ± 0.0 | 0.1 ± 0.0 | n.d.* | n.d.* |
| Sphalerite | 1.4 ± 0.2 | 1.0 ± 0.2 | 0.9 ± 0.2 | 0.2 ± 0.0 |
| Sulfosalts | 0.1 ± 0.0 | n.d.* | n.d.* | n.d.* |
| Sulfates | 0.1 ± 0.0 | 0.9 ± 0.3 | 0.9 ± 0.2 | 1.1 ± 0.1 |
| Fe carbonate | 2.4 ± 0.1 | 6.4 ± 1.2 | 7.0 ± 1.1 | 6.9 ± 1.2 |
| Other carbonates | 0.9 ± 0.1 | 1.1 ± 0.2 | 1.1 ± 0.3 | 0.6 ± 0.1 |
| Fe oxide | 0.1 ± 0.0 | 19.3 ± 2.8 | 40.1 ± 2.2 | 43.6 ± 2.4 |
| Fe sulfate | n.d.* | 5.1 ± 0.2 | 1.8 ± 0.3 | 1.5 ± 0.2 |
| Cu sulfate | n.d.* | 0.1 ± 0.0 | n.d.* | n.d.* |
| Cu oxide | n.d.* | n.d.* | n.d.* | n.d.* |
| Zn sulfate | n.d.* | n.d.* | n.d.* | 0.1 ± 0.0 |
| Zn oxide | n.d.* | n.d.* | n.d.* | n.d.* |

[b] mean content from 1000 bootstrap resampling simulations ± two standard deviations (σ) to show the 95 % confidence level

n.d.* not detected

MLA confirmed the observations made by QXRD analysis and showed that a significant amount of unreacted pyrite (12.0 wt %) was observed after MR at 400 °C, indicating insufficient roasting time and/or temperature. Fe sulfate is most abundant in the samples roasted at 400 °C (5.1 wt %), whereas the Fe oxide content doubles in the samples roasted at 500 °C and 600 °C (40.1 wt % and 43.6 wt %, respectively), compared to the 400 °C roasted sample (19.3 wt %). The SEM analysis illustrates the partial reaction of pyrite grains at lower roasting temperatures to form rims of Fe sulfate, Fe oxide and Fe carbonate, progressing to complete reaction of the grains at higher temperatures (Fig. 6). In particular the irregular surfaces of the Fe oxide phases are apparent. These observations confirm that the MR of pyrite particles progress according to the shrinking core model [43], whereby the reaction progress is controlled by the diffusion of reagents (i.e. oxygen) to the core of the pyrite particles and of reaction products (i.e. $SO_x$ gasses) to the particle surface.

Iron sulfate species can be present as $FeSO_4$ and/or $Fe_2(SO_4)_3$, likely depending on the composition of produced sulfur dioxide ($SO_2$ ) and sulfur trioxide ($SO_3$) in the furnace [44]. Iron oxides, specifically $Fe_2O_3$, as the final oxidation product become more evident at the higher roasting temperature. With MLA, it was not possible to distinguish ferrous sulfate from ferric sulfate, or hematite from magnetite.

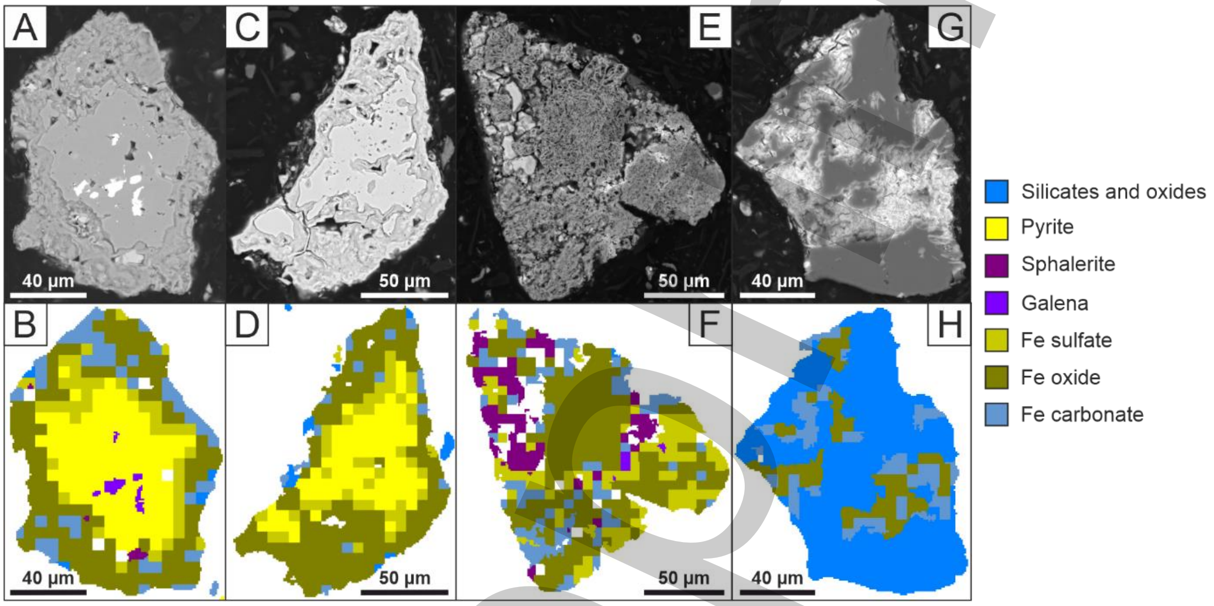

**Fig. 6** SEM–BSE images of iron species in MR samples (A, C: roasted at 400 °C; E: roasted at 500 °C; G: roasted at 600 °C) and corresponding false color images from MLA (B, D, F, H)

MLA of MR samples showed also that Cu sulfate and Zn sulfate phases were observed at 400 °C, which were then replaced by their respective oxides in the samples roasted at 500 °C and 600 °C. Fig. 7 and 8 display the reaction of Cu-bearing sulfides and Zn-bearing sphalerite, respectively. At lower roasting temperatures, partial reactions start to occur, with sulfate phases forming. At higher temperatures, oxide phases start to form. For example, Fig. 8E, G, F, H show reactions progressing around a crack in a sphalerite grain, from Zn oxide to Zn sulfate, further from the crack. Again, the irregular surfaces of the roasted phases are clear. In agreement with this observation, previous studies reported the formation of sulfates in the chalcopyrite starting to take place at 320 °C, while the decomposition into oxides at the temperature range of 500 °C to 550 °C [1], with mineral transformation as follows: $CuFeS_2 – Cu_2S – CuSO_4 – CuO.CuSO_4 – CuO – CuFe_2O_4$. Sphalerite (ZnS) also started to decompose to ZnO and $SO_2$ at 550 °C [45].

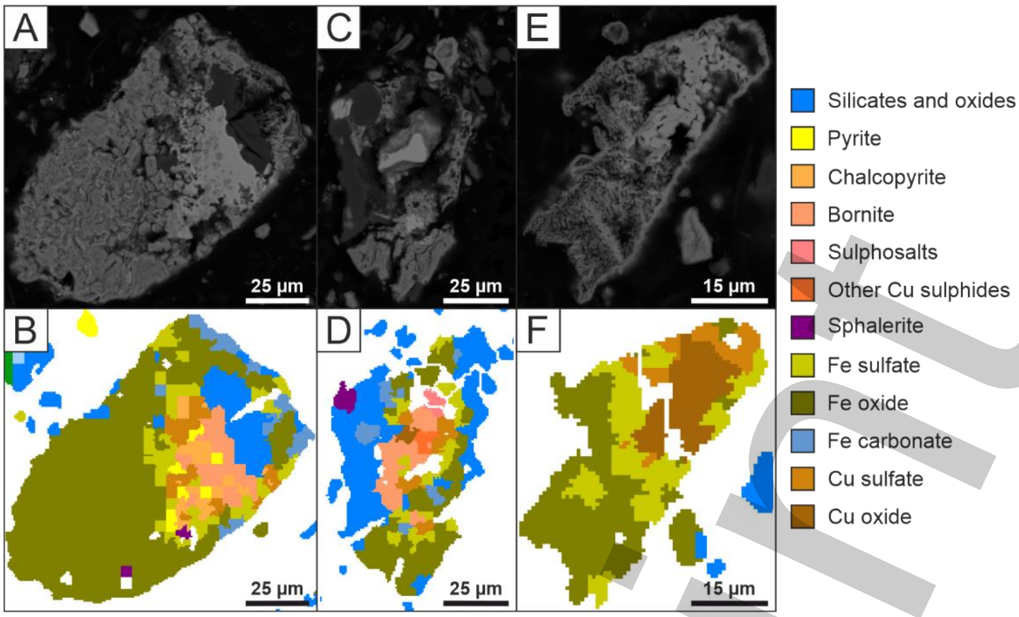

**Fig. 7** SEM–BSE images of copper species in MR samples (A: roasted at 400 °C; C: roasted at 500 °C; E: roasted at 600 °C) and corresponding false color images from MLA (B, D, F)

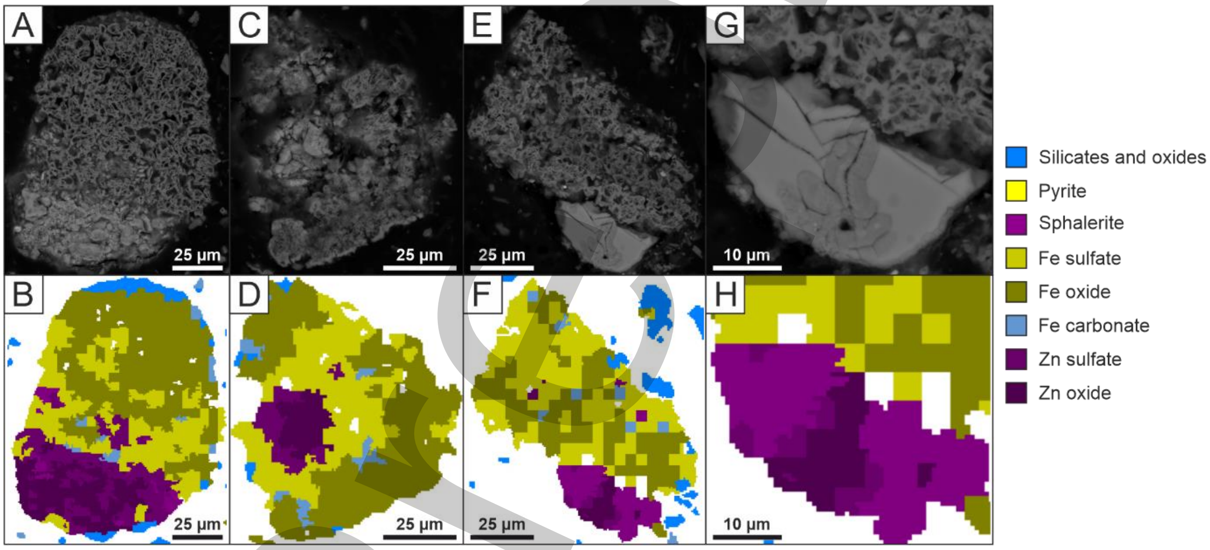

**Fig. 8** SEM–BSE images of zinc species in MR samples (A: roasted at 400 °C; C: roasted at 500 °C; E, G: roasted at 600 °C) and corresponding false color images from MLA (B, D, F, H)

Although no Pb sulfate or oxide phases were identified by MLA, lower roasting temperatures (400 °C to 500 °C) are expected to transform galena, as the main Pb-bearing mineral in the tailings, to lead sulfate ($PbSO_4$). Abdel-Rehim (2006) observed the intensive formation of $PbSO_4$ at 460 °C followed by the formation of basic lead sulfate ($PbSO_4 \cdot PbO$) at

580 °C [46]. Within the range of roasting temperatures tested in our study, only partial formation of lead oxide (PbO) is expected, as the complete sulfate decomposition occurs at 950 °C and above [46].

### Water Leaching Investigation

The influence of CR and MR on mineralogical changes of the Cu, Pb, Zn and As containing mineral phases could be indirectly assessed by water leaching since their respective sulfide, sulfate and oxide phases have significantly different solubilities. Fig. 9 displayed leaching efficiency ($E_L$) (left figure) and metal ion concentrations (right figure) for the CR and MR samples.

In general, the $E_L$ of Cu from CR samples lowers with increasing roasting temperature. The highest $E_L$ of 78 %, corresponding to 294 ppm of Cu ions in the PLS, was obtained at 400 °C. This suggests that Cu-bearing minerals in the tailings, mainly chalcopyrite, have mostly transformed from sulfide to sulfate phases starting at 400 °C, with minimal formation of oxides. The gradual decrease in $E_L$ for samples roasted at higher temperatures is ascribed to the more pronounced formation of insoluble Cu oxide phases. A similar trend can be seen in the $E_L$ of Fe, in which lower leaching efficiencies are obtained at higher roasting temperatures. Despite the overall low $E_L$ of Fe, the concentration of Fe in the PLS is much higher than that of Cu and the other metal ions due to its higher abundance in the starting material. In contrast to Cu and Fe, the $E_L$ of Zn raised with increasing roasting temperatures and reached a plateau at 550 °C, showing the highest $E_L$ of 62 %. As seen in the QXRD data, roasting at 600 °C indeed gave rise to lower mass percentage of Zn sulfates, as indicated by the Zn oxides formation which starts to occur at around this temperature subsequently leading to lower $E_L$. Similar to Zn, $E_L$ of As increased when higher temperature applied but already reached the plateau at 450 °C. For Pb, negligible leaching was observed at all temperatures which supposedly correlated with the formation of insoluble Pb sulfate and oxide.

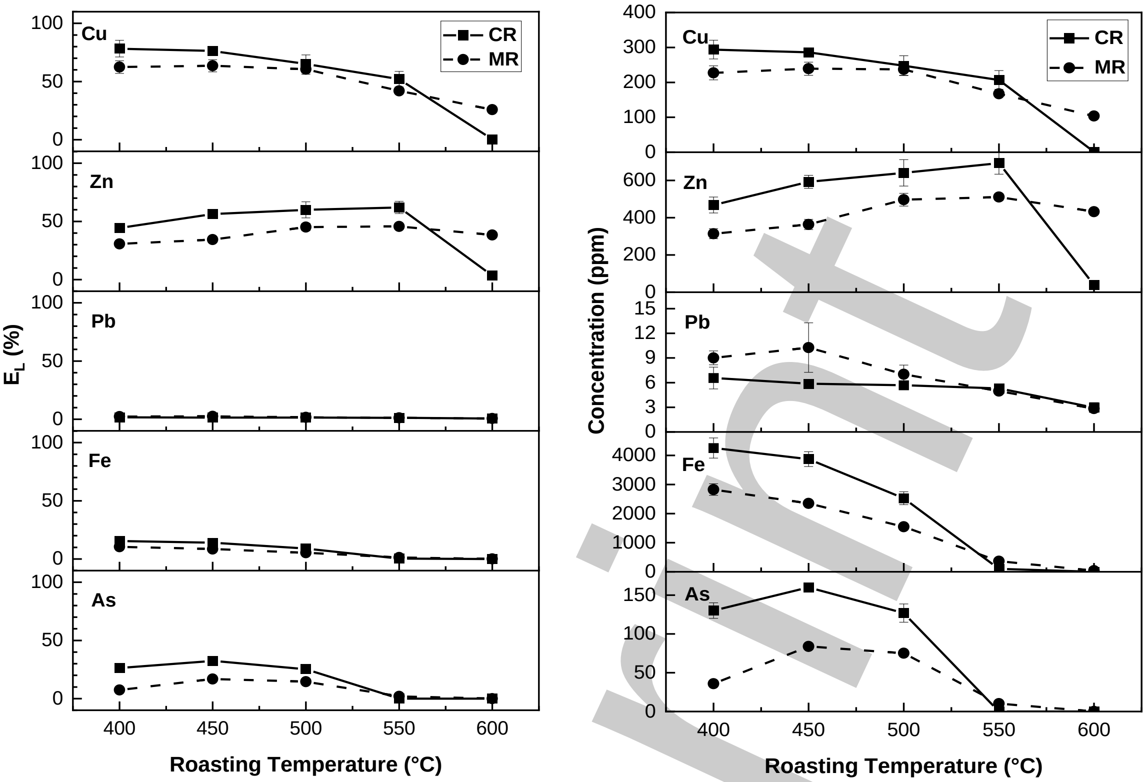

**Fig. 9** Water leaching assessment of roasted tailings (room temperature; 30 min; stirring speed 600 rpm; liquid/solid 10 mL · $g^{-1}$: leaching efficiency ($E_L$) of CR and MR samples (left) and metal ion concentrations of CR and MR samples (right)

The leaching patterns for MR samples were somewhat comparable with CR samples. However, the maximal $E_L$'s of Cu, Zn, Fe and As were respectively 63 %, 46 %, 11 % and 17 %; lower compared to CR samples. The lower $E_L$'s are explained by the faster sulfate-to-oxide phase transformations occurring during MR. Comparing the above QXRD data, this fast-paced oxides formation was marked by a lower amount of Zn and Fe sulfate, as well as a higher amount of hematite present in the MR samples, which caused their lower $E_L$'s. Meanwhile, the $E_L$ of Pb was not affected by the fast microwave heating; the formed Pb sulfate and oxide from roasting at 400-600 °C were water insoluble, explaining its negligible $E_L$ as in the case of CR samples.

pH and oxidation-reduction potential (ORP) measurements of the PLS supported the QXRD and water leaching results. As a function of roasting temperature, pH of the leachates increased at the higher roasting temperature (Fig. 10A). According to thermodynamic equilibrium calculations, the pH of the leaching solution is mainly governed by the presence of $Fe^{3+}$ in solution. Upon dissolution of $Fe_2(SO_4)_3$ it can react with water to form goethite (FeOOH) and sulfuric acid, even in acidic conditions, according to Eq. 12 [47].

$$Fe_2(SO_4)_3 + 4\ H_2O \rightarrow 2\ FeOOH + 3\ H_2SO_4 \qquad \text{(Eq. 12)}$$

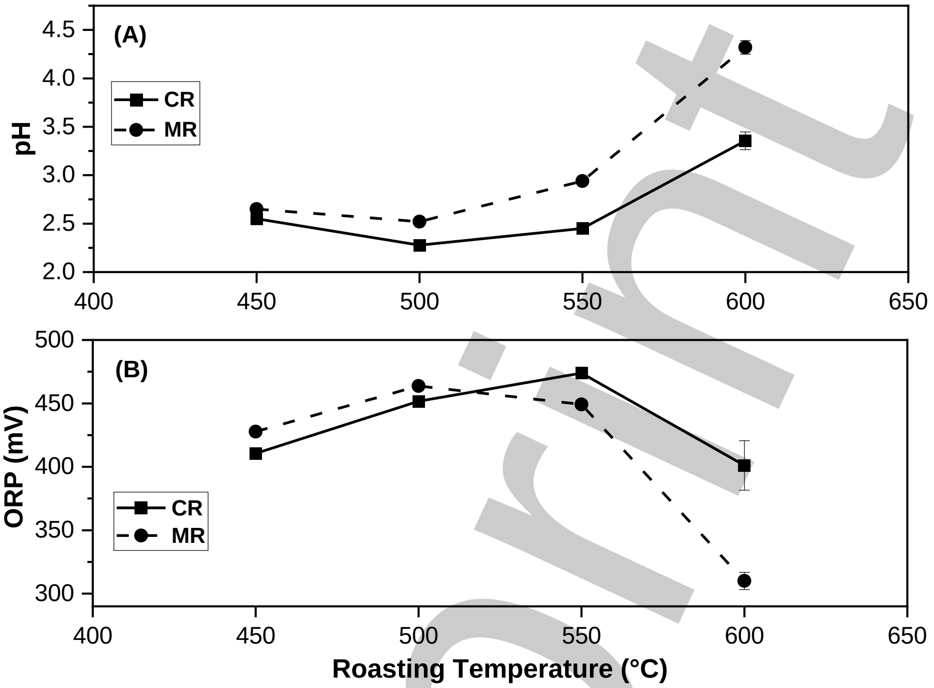

Fig. 10 (A) pH and (B) ORP measurement of the leachates obtained from samples roasted at different temperatures

By applying the QXRD derived mass percentage of $Fe_2(SO_4)_3$ in each roasted sample, the GEM module of HSC Chemistry allowed to calculate the pH of an aqueous solution containing the $Fe_2(SO_4)_3$ share of 1 g of roasted material in 10 mL of water. This allowed to plot, for the samples in which the presence of $Fe_2(SO_4)_3$ was observed by QXRD, the calculated pH versus the measured pH in the slurry of the same sample (Fig. 11). A clear correlation could be observed, showing that hydrolysis soluble Fe(III) species strongly controls the pH.

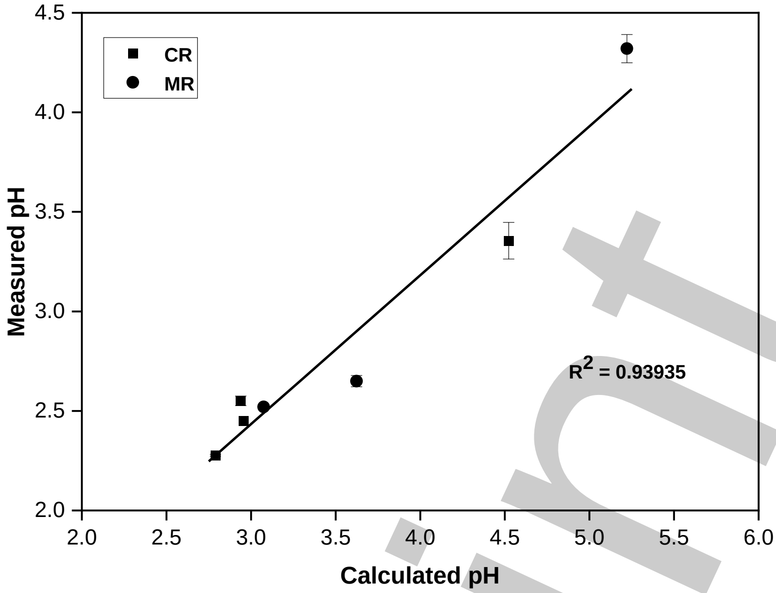

**Fig. 11** Calculated pH based on the $Fe_2(SO_4)_3$ content in roasted tailings *vs.* the measured pH of aqueous slurries (L/S = 10) of the same CR and MR tailing samples.

The slightly more acidic leachates for CR leachates with respect to MR confirm the more pronounced formation of sulfate species during CR. At the higher roasting temperatures (550 °C to 600 °C), the pH of the leachates becomes less acidic, as a result of the further decomposition of sulfate to less soluble oxide species. Similarly, the ORP values showed the increasing trend at 450 °C to 550 °C in CR and at 450 °C to 500 °C in MR (Fig. 10B), signaling the materials were more oxidized upon roasting. The gradual decrease of ORP values shown by samples roasted at higher temperatures indicated more insoluble oxides formed in the materials.

## Conclusions

Chemical and mineralogical characterization of the Neves Corvo tailings elucidated the following main bearing minerals of targeted metals: pyrite (Fe), chalcopyrite (Cu), sphalerite (Zn), galena (Pb) and arsenopyrite (As). Mineral phase transformations upon CR and MR were monitored by QXRD, MLA, Raman spectrometry, TG-DSC and MS analyses.

Pyrite was used as the representative sulfidic mineral phase to compare the roasting mechanism of sulfide minerals by conventional *versus* microwave-assisted heating. In the range of 400 °C to 550 °C, sulfide minerals in the tailings were mainly converted to sulfate minerals.

Increasing the roasting temperature above 550 °C resulted in further decomposition of the minerals into their respective oxides.

At similar roasting temperatures, CR resulted in a larger proportion of sulfate mineral phases ($Fe_2(SO_4)_3$), compared to MR. Whereas, MR gave a higher content of magnetite mineral phase ($Fe_3O_4$) compared to CR. The difference in these intermediate oxidation products indicates different roasting mechanisms for CR and MR. While CR induced indirect pyrite oxidation, MR triggered direct pyrite oxidation attributing to its faster heating rate.

The difference in mineral phases transformation during CR and MR was also confirmed for other metal containing sulfide phases by water leaching of the roasted materials. CR samples were shown to achieve a higher leaching efficiency of the metals Cu, Zn, As and Fe compared to MR samples when roasted at the same temperature. Overall, roasting at 500 °C to 550 °C for 1 hour gave the optimal condition for metal-leaching conditions for two reasons: i) soluble sulfate phases of the targeted metals (Cu and Zn) were more abundant and ii) the amount of soluble iron sulphate phases (i.e. Fe is an undesired element in solution) was lower in those temperature ranges.

## Compliance with Ethical Standards:

### Conflict of interest

On behalf of all authors, the corresponding author states that there is no conflict of interest.

## Acknowledgements

The authors thank SOMINCOR-Lundin Mining company and Alexandra G. Escobar for providing the sulfidic tailings. The authors also thank Myrjam Mertens for the help with XRD analysis. The research leading to these results has received funding from the European Community’s Horizon 2020 Program under Grant Agreement no. 812580 (MSCA-ETN SULTAN). This publication reflects only the authors’ view, exempting the Community from any liability. The Raman microscope was acquired via the FWO medium-scale research infrastructure (grant No I000718N).

## References

[1] S. Prasad, B. D. Pandey, 1998. Alternative processes for treatment of chalcopyrite - a review. Miner. Eng. 11, 8, 763–781. Doi: 10.1016/s0892-6875(98)00061-2.

[2] W. Wulandari, M. M. Kinda, R. Murida, T. W. Samadhi, 2020. The effect of alkali roasting pretreatment on nickel extraction from limonite ore by using dissolved $SO_2$-air.

Minerals 10, 701. Doi: 10.3390/min10080701.

[3] K. G. Thomas, A. P. Cole, 2016. Chapter 23 Roasting developments – especially oxygenated roasting, in: Gold ore processing. Ken Thomas & Murray Pearson, Ontario, 372–392. Doi: 10.1016/B978-0-444-63658-4.00023-2.

[4] F. Xia, A. Pring, J. Brugger, 2012. Understanding the mechanism and kinetics of pentlandite oxidation in extractive pyrometallurgy of nickel. Miner. Eng. 27–28, 11–19. Doi: 10.1016/j.mineng.2011.12.001.

[5] George Wang, 2016. Chapter 3 Nonferrous metal extraction and nonferrous slags, in: The utilization of slag in civil infrastructure construction. Woodhead Publishing, Cambridge, 35–61. Doi: 10.1016/b978-0-08-100381-7.00003-3.

[6] Mohammad Shamsuddin, 2016. Chapter 2 Roasting of sulfide minerals, in: Physical Chemistry of Metallurgical Processes. Springer, Cham, 39–69. Doi: 10.1002/9781119078326.

[7] J. Yu, Y. Han, Y. Li, P. Gao, 2020. Recent advances in magnetization roasting of refractory iron ores: a technological review in the past decade. Miner. Process. Extr. Metall. Rev. 41, 349–359. Doi: 10.1080/08827508.2019.1634565.

[8] T. Bai, H. yi Lei, Z. Lei, S. Li, 2020. Dearsenification of gold concentrates via microwave roasting. Canadian Metallurgical Quarterly 59, 60–66. Doi: 10.1080/00084433.2019.1665935.

[9] Kazi Haque, 1999. Microwave energy for mineral treatment processes - a brief review. Int. J. Miner. Process. 57, 1–24. Doi: 10.1016/s0301-7516(99)00009-5.

[10] Z. Peng, J. Y. Hwang, 2015. Microwave-assisted metallurgy. Int. Mater. Rev. 60, 30–63. Doi: 10.1179/1743280414Y.0000000042.

[11] N. K. Salakjani, P. Singh, A. N. Nikoloski, 2018. Acid roasting of spodumene: microwave vs. conventional heating. Miner. Eng. 138, 161–167. Doi: 10.1016/j.mineng.2019.05.003.

[12] K. Yang, S. Li, L. Zhang, J. Peng, W. Chen, F. Xie, A. Ma, 2016. Microwave roasting and leaching of an oxide-sulphide zinc ore. Hydrometallurgy 166, 243–251. Doi: 10.1016/j.hydromet.2016.07.012.

[13] K. Teimoori, F. Hassani, 2020. Twenty years of experimental and numerical studies on microwave-assisted breakage of rocks and minerals - a review. arxiv. 2011.14624, 1–43. https://arxiv.org/abs/2011.14624.

[14] M. L. Álvarez, J. M. Fidalgo, G. Gascó, A. Mendez, 2021. Hydrometalurgical recovery of Cu and Zn from a complex sulfide mineral by $Fe^{3+}/H_2SO_4$ leaching in the presence of carbon-based materials. Metals 11, 286. Doi: 10.3390/met11020286.

[15] J. Spooren, K. Binnemans, J. Björkmalm, K. Breemersch, Y. Dams, K. Folens, M. González-Moya, L. beth Horckmans, K. Komnitsas, W. Kurylak, M. Lopez, J. Mäkinen, S. Onisei, K. Oorts, A. Peys, G. Pietek, Y. Pontikes, R. Snellings, M. Tripiana, J. Varia, K. Willquist, L. Yurramendi, P. Kinnunen, 2020. Near-zero-waste processing of low-grade, complex primary ores and secondary raw materials in Europe: technology development trends. Resour. Conserv. Recycl. 160, 104919. Doi: 10.1016/j.resconrec.2020.104919.

[16] C. Falagán, B. M. Grail, D. B. Johnson, 2017. New approaches for extracting and recovering metals from mine tailings. Miner. Eng. 106, 71–78. Doi: 10.1016/j.mineng.2016.10.008.

[17] Robert Gordon, 2002. Production residues in copper technological cycles. Resour. Conserv. Recycl. 36, 87–106. Doi: 10.1016/S0921-3449(02)00019-8.

[18] M. Everaert, V. Lemmens, T. A. Atia, J. Spooren, 2020. Sulfidic mine tailings and marl waste rock as compatible resources in a microwave-assisted roasting process. J. Clean. Prod. 274, 122628. Doi: 10.1016/j.jclepro.2020.122628.

[19] Mustafa Özer, 2019. Cobalt and copper recovery from the ancient flotation tailings by selective sulfation roast - leaching process. J. Min. Metall. Sect. B Metall. 55, 315–324. Doi: 10.2298/JMMB190304043O.

[20] Marcin Wojdyr, 2010. Fityk: a general-purpose peak fitting program. J. Appl. Crystallogr. 43, 1126–1128. Doi: 10.1107/S0021889810030499.

[21] F. P. Araujo, N. Hulsbosch, P. Muchez, 2021. High spatial resolution Raman mapping of complex mineral assemblages: application on phosphate mineral sequences in pegmatites. J. Raman Spectrosc. 52, 690–708. Doi: 10.1002/jrs.6040.

[22] R. Fandrich, Y. Gu, D. Burrows, K. Moeller, 2007. Modern SEM-based mineral liberation analysis. Int. J. Miner. Process. 84, 310–320. Doi: 10.1016/j.minpro.2006.07.018.

[23] Ying Gu, 2003. Automated scanning electron microscope based mineral liberation analysis an introduction to JKMRC/FEI mineral liberation analyser. J. Miner. Mater. Charact. Eng. 2, 33–41. Doi: 10.4236/jmmce.2003.21003.

[24] T. Heinig, K. Bachmann, G. V. D. Boogaart, J. Gutzmer, 2015. Monitoring gravitational and particle shape settling effects on MLA sampling preparation. IAMG Conf. Proceed. F0404, Freiberg, 200–206.

[25] K. Bachmann, M. Frenzel, J. Krause, J. Gutzmer, 2019. Advanced identification and quantification of In-bearing minerals by scanning electron microscope-based image

analysis. Microsc. Microanal. 23, 527–537. Doi: 10.1017/S1431927617000460.

[26] M. Kern, R. Möckel, J. Krause, J. Teichmann, J. Gutzmer, 2017. Calculating the deportment of a fine-grained and compositionally complex Sn skarn with a modified approach for automated mineralogy. Miner. Eng. 116, 213–225. Doi: 10.1016/j.mineng.2017.06.006.

[27] R. Blannin, M. Frenzel, L. Tusa, S. Birtel, P. Ivascanu, T. Baker, J. Gutzmer, 2021. Uncertainties in quantitative mineralogical studies using scanning electron microscope-based image analysis. Miner. Eng. 167, 106836. Doi: 10.1016/j.mineng.2021.106836.

[28] H. Vogt, T. Chattopadhyay, H. J. Stolz, 1983. Complete first-order Raman spectra of the pyrite structure compounds $FeS_2$, $MnS_2$ and $SiP_2$. J. Phys. Chem. Solids 44, 869–873. Doi: 10.1016/0022-3697(83)90124-5.

[29] T. P. Mernagh, A. G. Trudu, 1993. A laser Raman microprobe study of some geologically important sulphide minerals. Chem. Geol. 103, 113–127. Doi: 10.1016/0009-2541(93)90295-T.

[30] E. E. Vázquez-Sánchez, A. Robledo-Cabrera, X. Tong, A. López-Valdivieso, 2020. Raman spectroscopy characterization of some Cu, Fe and Zn sulfides and their relevant surface chemical species for flotation. Physicochem. Probl. Miner. Process. 56, 483–492. Doi: 10.37190/PPMP/119763.

[31] Q. Zhu, N. J. Cook, G. Xie, B. P. Wade, C. L. Ciobanu, 2020. Arsenic-induced downshift of Raman band positions for pyrite. Econ. Geol. 115, 1589–1600. Doi: 10.5382/econgeo.4770.

[32] A. Pačevski, E. Libowitzky, P. Živković, R. Dimitrijević, L. Cvetković, 2008. Copper-bearing pyrite from the Čoka Marin polymetallic deposit, Serbia: mineral inclusions or true solid-solution?. The Can. Mineralogist 46, 249–261. Doi: 10.3749/canmin.46.1.249.

[33] J. M. R. S. Relvas, F. J. A. S. Barriga, A. Pinto, A. Ferreira, N. Pacheco, P. Noiva, G. Barriga, R. Baptista, D. De Carvalho, V. Oliveira, J. Munha, R. W. Hutchinson, 2002. The Neves Corvo deposit, Iberian Pyrite Belt, Portugal: impacts and future 25 years after the discovery," SEG Spec. Publ. 9, 155–176.

[34] M. Ozer, E. Acma, G. Atesok, 2017. Sulfation roasting characteristics of copper-bearing materials. Asia-Pacific J. Chem. Eng. 12, 365–373. Doi: 10.1002/apj.2078.

[35] Ž. D. Živković, N. Mitevska, V. Savović, 1996. Kinetics and mechanism of the chalcopyrite - pyrite concentrate oxidation process. Thermochim. Acta 282–283, 121–130. Doi: 10.1016/0040-6031(96)02883-3.

[36] J. P. Briggs, R. R. Hudgins, P. L. Silveston, 1976. The fragmentation of $SO_3$ in electron

impact ionization sources. Int. J. Mass Spectrom. Ion Phys. 20, 1–5. Doi: 10.1016/0020-7381(76)80027-7.

[37] B. Munson, D. Smith, C. Polley, 1977. The mass spectrum, proton affinity and ion-molecule reactions of $SO_3$. Int. J. Mass Spectrom. Ion Phys. 25, 323–326. Doi: 10.1016/0020-7381(77)80058-2.

[38] J. E. Pahlman, G. W. Reimers, 1986. Thermal gravimetric analysis of pyrite oxidation at low temperature. Report of Investigation 9059. United States, Bur. Mines.

[39] J. G. Dunn, G. C. De, 1989. The effect of experimental variables on the mechanism of the oxidation of pyrite, Part 1 Oxidation of particles less than 45 µm in size. Thermochimica Acta 145, 115–130. Doi: 10.1016/0040-6031(89)85131-7.

[40] J. H. Huang, N. A. Rowson, 2001. Heating characteristics and decomposition of pyrite and marcasite in a microwave field. Miner. Eng. 14, 9, 1113–1117.

[41] X. Zhang, J. Kou, C. Sun, 2019. Comparison of microwave and conventional heating methods for the thermal decomposition of pyrite under different heating temperatures. J. Anal. Appl. Pyrolysis 138, 41–53. Doi: 10.1016/j.jaap.2018.12.002.

[42] M. Diaz, I. Amaya, R. Correa, 2016. Microwave enhanced roasting for pyrite ore samples with dielectric properties strongly dependent on temperature. Ing. Univ. Bogotá 20, 63–84. Doi: 10.11144/javeriana.iyu20-1.merp.

[43] Octave Levenspiel, 1999. Chapter 25 Fluid-particle reactions: kinetics, in: Chemical Reaction Engineering. John Wiley & Sons, New York, 566–588.

[44] G. Hu, K. Dam-Johansen, S. Wedel, J. P. Hansen, 2006. Decomposition and oxidation of pyrite. Prog. Energy Combust. Sci. 32, 295–314. Doi: 10.1016/j.pecs.2005.11.004.

[45] D. Amalia, T. Wahyudi, Y. Dahlan, 2018. The natures of zinc sulfide concentrates and its behavior after roasting process. Indones. Min. J. 21, 99–112. Doi: 10.30556/imj.vol21.no2.2018.698.

[46] A. M. Abdel-Rehim, 2006. Thermal and XRD analysis of Egyptian galena. J. Therm. Anal. Calorim. 86, 393–401. Doi: 10.1007/s10973-005-6785-6.

[47] K. Kandori, T. Shigetomi, T. Ishikawa, 2004. Study on forced hydrolysis reaction of acidic $Fe_2(SO_4)_3$ solution - structure and properties of precipitates. Colloids Surfaces A Physicochem. Eng. Asp. 232, 19–28. Doi: 10.1016/j.colsurfa.2003.10.003.